Natural Hazards
and Earth System
Sciences
Discussions

Leveraging multi-model season-ahead streamflow forecasts to trigger advanced flood preparedness

Colin Keating[1,2], Donghoon Lee[1,3], Juan Bazo[4,5], Paul Block[1]

[1]Department of Civil and Environmental Engineering, University of Wisconsin-Madison, Madison, USA
5 [2]Nelson Institute for Environmental Studies, University of Wisconsin-Madison, Madison, USA
[3]Climate Hazards Center, Department of Geography, University of California, Santa Barbara, USA
[4]Red Cross Red Crescent Climate Centre, The Hague, 2521 CV, the Netherlands
[5]Universidad Tecnológica del Perú (UTP), Lima, Perú

Correspondence to: Colin Keating (ckeating2@wisc.edu)

10 **Abstract.** Disaster planning has historically allocated minimal effort and finances toward advanced preparedness, however evidence supports reduced vulnerability to flood events, saving lives and money, through appropriate early actions. Among other requirements, effective early action systems necessitate the availability of high-quality forecasts to inform decision making. In this study, we evaluate the ability of statistical and physically based season-ahead prediction models to appropriately trigger flood early preparedness actions based on a 75% or greater probability of surpassing the 80th percentile

15 of historical seasonal streamflow for the flood-prone Marañón River and Piura River in Peru. The statistical prediction model, developed in this work, leverages the asymmetric relationship between seasonal streamflow and the ENSO phenomenon. Additionally, a multi-model (least squares combination) is also evaluated against current operational practices. The statistical and multi-model predictions demonstrate superior performance compared to the physically based model for the Marañón River by correctly triggering preparedness actions in all four historical occasions. For the Piura River, the

20 statistical model proves superior to all other approaches, and even achieves an 86% hit rate when the required threshold exceedance probability is reduced to 50%, with only one false alarm. Continued efforts should focus on applying this season-ahead prediction framework to additional flood-prone locations where early actions may be warranted and current forecast capacity is limited.

1 Introduction and motivation

25 Globally, flood catastrophes lead all natural hazards in terms of mortality and cause billions of dollars in damages annually (Doocy et al., 2013; IFRC, 2020; Lee et al., 2018; Munich RE, 2012, 2018). Government agencies and relief organizations have historically prioritized disaster relief, allocating the majority of financial resources to response efforts in a reactionary mode, in lieu of pre-disaster preparedness (Perez et al., 2016). However, forecast based early action (FbA) initiatives are now recognized as a critical component of disaster risk reduction (*World Disasters Report 2009: Focus on early warning*,

30 *early action*, 2009). While no strict definition for FbA exists, the term generally refers to initiatives that provide assistance

Natural Hazards
and Earth System
Sciences
Open Access
EGU
Discussions

and allocation of resources to prepare in advance of disasters based on hydro-climate forecasts (Wilkinson et al., 2018). Empirical evidence demonstrates that actions taken in advance of a disaster can reduce loss of life and result in cost savings for relief organizations (Aguirre et al., 2019; Braman et al., 2013; Golnaraghi, 2012; Gros et al., 2019).

35 Forecast performance, uncertainty and hazard type contribute to the range and extent of potential early actions available. In 2013, a near-certain forecast prompted the evacuation of approximately 400,000 people in advance of Cyclone Phailin in India given a lead time of just four days (Harriman, 2014). While longer lead times allow for a greater range of potential early actions (Bazo et al., 2019), this must be balanced against corresponding increases in forecast uncertainty. To address this tradeoff, disaster managers seek low-regret actions, potentially in combination with a mechanism to halt early actions if

40 the threat of a disaster sufficiently drops, and thus avoid unnecessary costs (Wilkinson et al., 2018). While FbA was initially applied to acute and slowly evolving threats like tropical cyclones and droughts, more recent efforts have targeted hydrological threats including extreme rainfall and flooding (e.g., Gros et al., 2019). For example, in West Africa in 2008, preparatory actions, including prepositioning relief supplies and volunteer training, initiated based on a season-ahead forecast of above-average rainfall and high likelihood of floods, resulted in fewer deaths and lower response costs compared

45 to previous flood events when no early action was taken (Braman et al., 2013).

The question of when to initiate FbA requires integrating a hazard forecast with vulnerability and exposure information to estimate the impact of an extreme event. One commonly used method to trigger early action is to define a forecast threshold above which impacts are likely to occur based on historical data (Wilkinson et al., 2018). In London, actions to reduce

50 vulnerability for high-risk groups, such as ensuring indoor temperatures are below 26°C, are triggered when temperatures are forecast to be at least 32°C during the day and at least 18°C at night (Public Health London, 2018). This method accounts for the probabilistic nature of forecasts by requiring a predetermined level of forecast confidence; in London, a 60% probability of reaching the temperature thresholds is required.

55 **Table 1:** Contingency table demonstrating potential outcomes of forecast based action.

	Extreme Event	**No Extreme Event**
Early Action	*Worthy action*	*Action in vain*
No Early Action	*Failure to act*	*Worthy inaction*

When linking early action based on probabilistic forecasts to the occurrence of extreme events, four scenarios are possible (Table 1) where worthy action and worthy inaction are preferred. The risk of acting in vain, when early action is initiated but an extreme event fails to materialize (Lopez et al., 2019), is often viewed as a major barrier to scaling up FbA (Tanner et al.,

60 2019). However, studies have found that, when compared to a late response, early action is almost invariably cheaper: a late response can be two to six times more costly than actions in vain (Cabot Venton et al., 2012). Additionally, financial based

actions such as unconditional cash disbursements targeting vulnerable households can yield a benefit regardless of whether or not the event occurs (Wilkinson et al., 2018). Forecast models that proficiently predict extreme events at lead times permitting early action are critical for minimizing false positives and false negatives. In addition to short term weather

65   forecasts which are commonly viewed as skillful, medium to long range climate forecasts have also been demonstrated to improve preparedness protocols, resulting in reduced mortality, morbidity, and resource demands (Braman et al., 2013), yet their applications have been limited predominantly as a result of moderate forecast performance and significant uncertainty.

Hydrologic models are essential components of flood early warning systems and can be typically divided into two

70   categories. Physically based (or dynamical) models simulate physical processes such as infiltration and runoff to produce streamflow predictions and are often forced with climate predictions downscaled from general circulations models (GCMs) or numerical weather models. Statistical (also called empirical or data-driven) models forgo the parameterization of complex physical processes in favor of understanding the lagged relationships between precipitation or streamflow and antecedent land, atmosphere and ocean conditions. Statistical and physical models have been successfully applied to seasonal prediction

75   of hydrologic variables including precipitation and streamflow (e.g. Badr, et al., 2013; Block & Rajagopalan, 2009). Both frameworks have their own set of advantages and disadvantages with prediction skill varying according to season and location (Infanti & Kirtman, 2014). While statistical models are not intended to provide a complete understanding of the hydro-climate system, they offer an appealing complement to physically based models by focusing solely on the prediction variable of interest (Zimmerman et al., 2016).

80

This study evaluates multiple season-ahead forecast approaches, namely locally tailored statistical and existing global-scale physical models, to individually and collectively inform advanced flood preparedness actions, using Peru as a case study. Typically, only physically based forecast approaches are used operationally, however augmenting with a locally tailored statistical forecast may considerably improve forecast performance and opportunities for preparedness.

85   2 Case study in Peru

2.1 Flood impacts in Peru

Peru experiences catastrophic flooding with relative frequency, resulting in significant adverse economic and health impacts. In northwest Peru, flooding caused by extreme rainfall during El Niño events in 1982-83, 1997-98 and the 2017 "coastal El Niño" each incurred damages exceeding USD$5 billion (in 2020 dollars) and collectively resulted in over 1000 deaths

90   (French & Mechler, 2017; Venkateswaran et al., 2017). Flooding in the Peruvian Amazon basin affected over 300,000 people in 2012 (IFRC, 2012) and over 100,000 people in 2015 (IFRC, 2015). Floods prevent access to safe drinking water, disrupt livelihoods centered around farming and fishing, and can force residents to relocate from low-lying areas (IFRC,

2019). Health impacts of extreme flooding include increased incidence of acute diarrheal disease, arboviral diseases, malaria, and water-borne diseases (Caviedes, 1984; IFRC, 2019).

2.2 Hydroclimatology of Peru

While floods are common throughout many regions of Peru, climate and hydrology vary dramatically. The hydroclimatology of Peru is broadly characterized by a disruption of tropospheric flow caused by the Andes cordillera, which maintains an arid climate along the Pacific coast and wet conditions in the Amazon basin to the east (Garreaud et al., 2009). Particularly along coastal Peru, a major source of interannual variability in precipitation and temperature is controlled by the El Niño Southern Oscillation (ENSO) phenomenon, a system of ocean-atmosphere feedbacks in the tropical Pacific (Garreaud et al., 2009). In the southern coastal region, the warm, positive phase of ENSO (El Niño) is associated with below average precipitation (Wu et al., 2018). In northwest Peru, strong El Niño years are often associated with above average precipitation, most notably during the 1982-83 and 1997-98 El Niño events which coincided with extreme rainfall and flooding (Bayer et al., 2014). However, the impacts of similarly intense El Niño events are variable. Despite very strong El Niño conditions in 2015-2016, rainfall and flood impacts in Peru were minimal (French & Mechler, 2017; Ramirez & Briones, 2017; Venkateswaran et al., 2017). El Niño events can span the equatorial Pacific region (e.g. 1982-83, 1997-98) or they can be confined to the coast of northern Peru and Ecuador (Ramirez & Briones, 2017). The latter type is known as a "coastal El Niño" or "El Niño costero" and occurred in 1925 and 2017, in both cases resulting in extreme rainfall and flooding (Ramirez & Briones, 2017; Takahashi & Martínez, 2017). While El Niño conditions are associated with extreme events along the coast, La Niña (cool, negative phase of ENSO) conditions can also produce slightly higher than average streamflow (see Figure 2b).

In the Amazon basin, while the literature has described relationships between climate patterns and hydrometeorological variables, the way in which climate variables influence flood risk remains understudied (Towner et al., 2020) as a result of the nonlinear relationship between precipitation and streamflow (Stephens, Day, Pappenberger, & Cloke, 2015). Hydrometeorological regimes in the Amazon basin are diverse and are driven by seasonal warming of the northern and southern hemispheres and the migration of the Intertropical Convergence Zone (Espinoza Villar et al., 2009). Precipitation in the Peruvian austral summer (DJFM) is dominated by the South American Monsoon season which enhances the north Atlantic trade wind (Zhou & Lau, 1998) as well as by deep convection that recycles moisture over Amazonia (Garreaud et al., 2009). El Niño conditions and above-average sea surface temperatures (SST) in the tropical north Atlantic, south Atlantic, and Indian Oceans are associated with decreased rainfall in the northern portion of the basin and increased rainfall in the south (Marengo, 2004). La Niña conditions are weakly associated with increased precipitation in the western Amazon basin (Garreaud et al., 2009).

2.3 Flood early action plan

In October 2019, the International Federation of Red Cross and Red Crescent Societies (IFRC) approved an Early Action
125 Plan (EAP) submitted by the Peruvian Red Cross for flooding in the Peruvian Amazon. The plan is based in part on an
extension of the Global Flood Awareness System (GloFAS) called GloFAS-seasonal, a global streamflow forecast model
developed by the European Centre for Medium-Range Weather Forecasts (ECMWF) that couples seasonal climate forecasts
from GCMs to a physically based hydrology model (Emerton et al., 2018). Early actions, which involve the prepositioning of
supplies and release of funds, are triggered when 75% of GloFAS ensemble members forecast streamflow above the 80th
130 percentile (IFRC, 2019) at a 45-day lead time. Because GloFAS exhibits only modest forecast skill in Peru when detecting
floods at short lead times (Bischiniotis et al., 2019), there is an opportunity to leverage complementary prediction
frameworks to improve forecast performance. Similarly, an EAP is in development for the Piura basin in coastal northwest
Peru to address extreme precipitation and flooding.

2.4 Case study locations

135 Study locations prone to riverine flooding were identified by collaborators at the Red Cross Climate Center in Lima, Peru,
and the EAPs, namely the Marañón River at San Regis and the Piura River at Puente Sánchez Cerro (Figure 1). The
Marañón is a tributary to the Amazon River, east of the Andes, with a basin covering approximately one-half (362,000 km^2)
of the Peruvian Amazon River basin. Here, tropical lowland forest (below 600 m elevation) is the dominant ecozone
followed by tropical montane forest (above 600 m elevation) (Kvist & Nebel, 2001). The Piura River basin above Puente
140 Sánchez Cerro is significantly smaller in size (7,435 km^2) consisting of tropical shrubland and tropical mountain systems and
is generally classified as arid with precipitation averaging less than 50 mm/year for elevations below 500 m (FAO 2001;
Rodriguez et al., 2005). Throughout this paper, the names of the monitoring stations will be used to describe the stations and
the basins they delimit.

2.5 Streamflow variability

145 Daily streamflow data for each location (1999-2017 at San Regis, 1971-2017 at Puente Sánchez Cerro) was provided by the
Peruvian Meteorological Agency, El Servicio Nacional de Meteorología e Hidrología del Perú (SENAMHI). Monthly mean
streamflow at Marañón exhibits a statistically significant autocorrelation at one- and two-month lags, however monthly
streamflow at Piura exhibits no significant autocorrelation. This is predominantly an effect of catchment size and watershed
memory, and an important feature for streamflow prediction.

150

The high flow season during which floods are likely to occur is computed using an approach modified from Lee et al.
(2015). This season is defined as the three consecutive months with the largest combined number of days having streamflow
values in the top 1% of all days in the historical record. For Marañón, this high flow season is March, April and May

(MAM); for Piura, it is February, March and April (FMA). Testing this approach with a slightly lower threshold to define
155   high flow days (3% and 5%) returns the same high flow season, further validating the seasons selected. The high flow season
for Marañón identified via this methodology is similar to the IFRC's characterization of flood season in the Amazon basin as
running from December to April (IFRC, 2019). At Marañón, all daily observations in the top 1% occurred in MAM and the
annual maximum occurred in MAM in 17 out of 19 years; at Piura, 87% of daily observations in the top 1% occurred in

160   **Figure 1:** Case study locations with catchment boundaries delimited in red. Made with Natural Earth (naturalearthdata.com).

FMA while the annual maximum discharge occurred in FMA in 40 out of 47 years. Clearly, high flow conditions occur
outside these seasons, however in this study these will not be captured as the focus is on the likelihood of high flow
conditions within the target season only.

3 Statistical approach to season-ahead streamflow prediction

165   **3.1 Potential local-scale predictor variables**

Ocean-land-atmospheric variables representative of slowly evolving hydro-climatic conditions offer prospects for predicting
streamflow from a season-ahead lead. This includes considering pre-season large-scale ocean-atmosphere teleconnections

Natural Hazards
and Earth System
Sciences
Discussions

Open Access

EGU

and basin-scale hydrologic processes such as observed streamflow, precipitation, soil moisture, and temperature (Table 2). Predictions of seasonal average streamflow are issued on the first day of the three-month high flow season identified in Sect.

170   2, leveraging predictors based on values in the preceding months. Potential predictors must be statistically significantly correlated with streamflow (p < 0.1) to be retained.

Precipitation data used in this study leverages the Peruvian Interpolation data of SENAMHI's Climatological and hydrological Observations (PISCO) v2.1 dataset (Aybar et al., 2020), provided by SENAMHI and accessed via the

175   International Research Institute for Climate and Society (IRI; http://iridl.ldeo.columbia.edu). PISCO contains monthly and daily precipitation at a 0.1 degree grid resolution from 1981 to 2017, and is based on the Climate Hazards group InfraRed Precipitation with Stations (CHIRPS; Funk et al., 2015) quasi-global precipitation product calibrated with SENAHMI station data. Basin-averaged precipitation over January-February is included as a potential predictor for the Marañón at San Regis (Table 2). January and February precipitation each also correlate significantly, though less so compared to the January-

180   February average; to maintain model parsimony we included only the latter as a potential predictor. The Piura catchment is approximately 2% the size of the Marañón and only basin-averaged precipitation in January significantly correlates with streamflow (Table 2).

Soil moisture data (0.5°, monthly) is provided by the National Oceanic and Atmospheric Administration (NOAA) Climate

185   Prediction Center (Fan & van den Dool, 2004). Atmospheric moisture transport can occur over long distances and across catchment boundaries; to capture potential signals of soil moisture on streamflow variability, a principal component analysis is conducted on one-month ahead gridded soil moisture across northern South America, and the first principal component (PC) is retained as a potential predictor. Basin-averaged mean air temperature in the month prior to the forecast, provided by the NOAA (https://psl.noaa.gov/) is also considered (Table 2).

190

Given that the Piura basin is relatively small and within-season precipitation is an important contributor to seasonal streamflow, FMA precipitation (mm/day) predictions derived from the mean of two GCM members (NASA GEOSS2S and NCEP CFSv2) of the North American Multi-Model Ensemble (NMME) (Kirtman et al., 2014) are also evaluated. The two models have exhibited superior performance in terms of RMSE, temporal correlation, and Heidke Skill Score in northwest

195   Peru compared to other NMME models when simulating January, February and March precipitation across lead times of one to six months (Wang & Vavrus, 2020). Individually, each model's FMA precipitation prediction correlates with streamflow at 0.76; when averaged, correlation increases to 0.84 (Table 2).

Natural Hazards
and Earth System
Sciences
Discussions

200 **Table 2:** The suite of potential predictor variables and their Pearson correlation coefficient with FMA streamflow at Piura at Puente Sánchez Cerro and MAM streamflow at Marañón at San Regis; * indicates statistically significant correlations ($p < 0.05$). SST and SLP predictor locations are determined by NIPA and correlations are presented by phase.

Potential Predictor	Spatial Region	Time Frame		Pearson Correlation with Streamflow				
		Piura	Marañón	Piura			Marañón	
Streamflow	-	J	F	0.84*			0.84*	
Precipitation	Basin-Avg	J	JF	0.88*			0.68*	
Soil Moisture	1st PC of statistically significant ($p < 0.05$) regions within 12N to 23S, 35W to 81.5W	J	F	0.69*			0.74*	
Air Temperature	Basin-Avg	J	F	0.26			0.11	
GCM Precipitation Forecast	4.5S to 5.5S, 79.5W to 80.5W	FMA	-	0.84*			-	
				El Niño	Neutral	La Niña	El Niño	La Niña
Sea Surface Temperature	1st PC of NIPA-identified regions	NDJ	DJF	-0.79*	-0.90*	0.85*	-0.93*	-0.80*
Sea Level Pressure	1st PC of NIPA-identified regions	J	F	-0.82*	-0.74*	0.79*	0.90*	-0.72*

3.2 Potential large-scale predictor variables

205 A common approach for identifying SST regions for use as predictors is to search for stable correlations between the predictand (streamflow in this case) and SSTs over a moving window of historical data (Gámiz-Fortis et al., 2010; Ionita et al., 2015). However, the state of ENSO can influence the mean state of the atmospheric-oceanic system, which in turn affects the relevant teleconnections between SSTs and precipitation or streamflow (Zimmerman et al., 2016). This asymmetric relationship between ENSO and streamflow may prove challenging from a traditional modeling perspective. At our study

210 sites, the distributions of seasonal streamflow shift and change shape according to the state of ENSO, though significant variability within each phase exists (Figure 2). A Nino Index Phase Analysis (NIPA; Giuliani et al., 2019; Zimmerman et al., 2016) approach is advantageous in such cases, capturing the variance and signals within each phase separately, and thus addressing the overall asymmetric challenges.
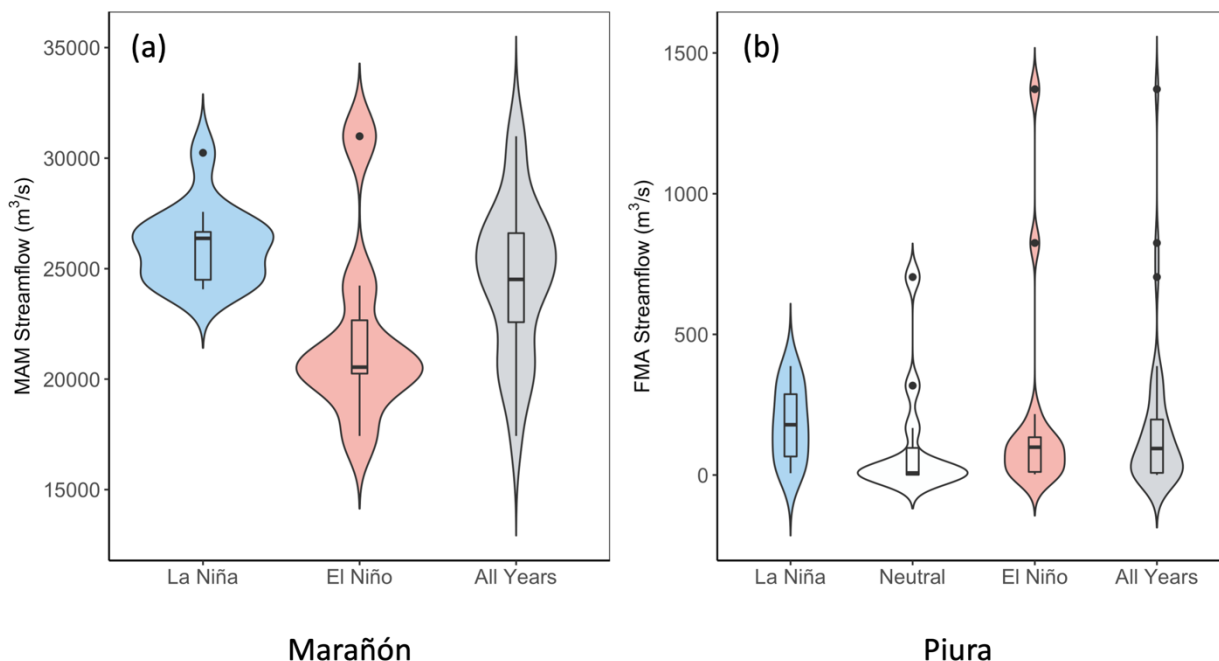
Figure 2: Violin plots of seasonal streamflow by ENSO phase. For the Marañón River at San Regis (n=19), twelve historical years are classified as La Niña conditions (MEI ≤ 0) and seven are classified as El Niño conditions (MEI > 0). For the Piura River at Puente Sánchez Cerro (n=36), eleven years are classified as La Niña (MEI ≤ -0.5), eleven as neutral (-0.5 < MEI < 0.5), and fourteen as El Niño conditions (MEI ≥ 0.5).

The approach proposed by Zimmerman et al. (2016) is adopted to select global SST and Sea Level Pressure (SLP) regions exhibiting strong teleconnections with streamflow at our study sites. The selection of these regions is conditioned on the preseason state of ENSO (NDJ for Piura and DJF for Marañón) as represented by the average Multivariate ENSO Index (MEI) value (Wolter & Timlin, 2011). Historical years are categorized according to the preseason average value of MEI. For this analysis, three categories are selected for Piura and two for Marañón (Figure 2). While including more bins may potentially provide additional unique streamflow information by further distinguishing climate system states, this needs to be balanced against available observational data. For Piura, the three categories are generally representative of El Niño, La Niña or neutral conditions, per NOAA's definition ("Equatorial Pacific Sea Surface Temperatures," n.d.). The short historical dataset at Marañón at San Regis limits categorizing into two phases delineated as positive and negative MEI values. (A two-phase model for Piura was also tested but did not materially change model performance.) For years classified within each phase, observed target season streamflow is correlated with global pre-season SSTs from the NOAA Extended Reconstructed Sea Surface Temperature V3b dataset (Smith et al., 2008), a global gridded dataset of monthly mean SSTs at a two-degree resolution from 1854 to present accessed via the IRI data library. Of the SST regions statistically significantly

correlated with streamflow (Figure 3), the first and second PC is extracted as a potential predictor in the statistical model. For Piura (Marañón) the first and second PCs explain 83% and 7% (84% and 6%) of the variance respectively and only the first PC significantly correlates with streamflow. Selecting SST regions based on the preseason state of the Niño 1+2

235   anomaly index instead of MEI did not materially change results at Piura.

Given that SLP evolves more quickly than SSTs, only the single month values prior to the target season are evaluated, otherwise the process mirrors SST selection. SLP data is from the NCEP/NCAR Climate Data Assimilation System I (Kalnay et al., 1996) and accessed via the IRI data library.
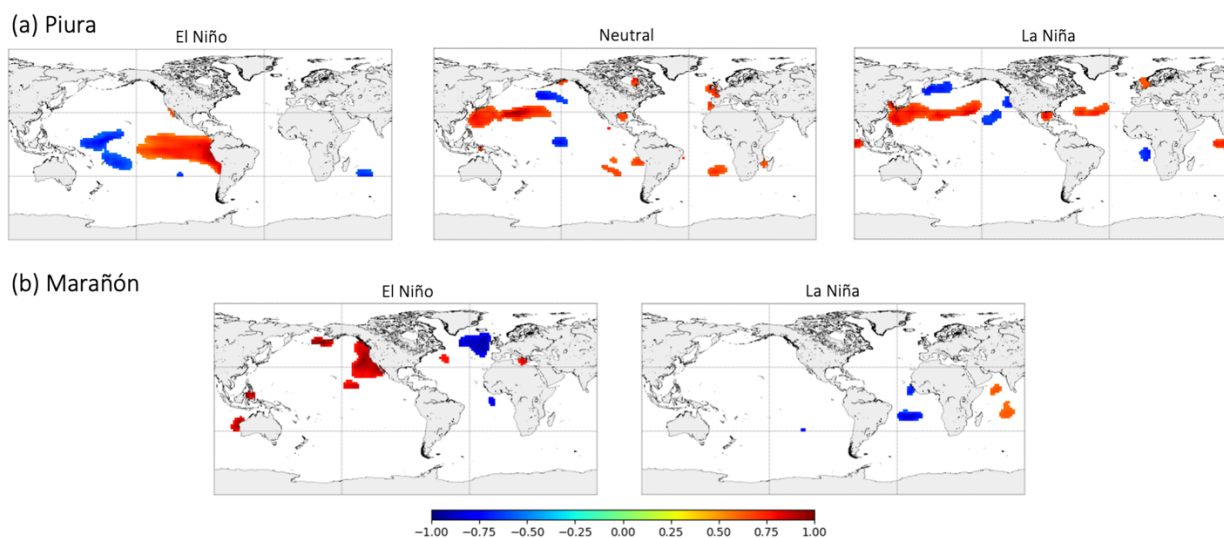
240

Figure 3: Correlation maps of seasonal streamflow at a) Piura (FMA) and b) Marañón (MAM) with pre-season SSTs by ENSO phase. Only regions statistically significantly correlated at p<0.05 are included.

3.3 Statistical prediction model

For each location, a principal component regression (PCR; coupled principal component analysis and multiple linear

245   regression) framework is adopted to predict seasonal streamflow by ENSO phase. This results in two PCR "submodels" for the Marañón River at San Regis and three for the Piura River at Puente Sánchez Cerro where the submodel used for prediction in a given year is selected based on preseason MEI. For example, in 1998 the preseason (NDJ) average MEI value is 2.43 so the positive phase submodel is selected to predict Piura River FMA streamflow. In each submodel, relevant predictors by ENSO phase are included; predictor variable types may be included in some submodels and not others,

250   depending on their correlation with streamflow in that phase. A subset of PCs is retained for input into the multiple linear regression, given as:

$$y_t = \beta_0 + \beta_1 x_{1,t} + \cdots + \beta_n x_{n,t} + e , \qquad (1)$$

where y_t is observed seasonal streamflow in year t, β_0 is a constant, $\beta_1 \dots \beta_n$ are regression coefficients, $x_{1,t} \dots x_{n,t}$ are the PCs retained, and e is the residual or error. There are numerous methods for selecting the appropriate number of PCs to retain; here, the first two PCs are retained unless the model has two or fewer predictors, and then only the first PC is retained.

To favor parsimonious models, the optimal subset of predictors is selected according to the generalized cross-validation (GCV) score function (P. Block & Rajagopalan, 2007), given as:

$$GCV = \frac{\Sigma_{t=1}^{N} \frac{e_t^2}{N}}{\left(1 - \frac{m}{N}\right)^2},$$ (2)

where e_t is the model error, or difference between observed and predicted values, m is the number of predictors, and N is the number of data points (time steps). GCV penalizes the use of additional predictors; lower scores indicate optimal tradeoff between minimizing prediction errors and the number of predictors included.

To evaluate the performance of each submodel, a drop-one-year cross validation hindcast is constructed, refitting the regression coefficients each year, to produce a deterministic seasonal streamflow prediction. When model residuals are normally distributed, according to the Shapiro-Wilk test with alpha=0.05, an error distribution is created by taking 1000 random samples. Otherwise, an error distribution is derived by directly sampling the model residuals with replacement 1000 times. The resulting error distribution is then added to the cross-validated deterministic prediction to create a probabilistic streamflow prediction. This process is repeated for each year to create a probabilistic hindcast for all years in the submodel. Hindcasts from each submodel are subsequently joined to create a full observational period hindcast.

3.4 GloFAS and multi-model predictions

Predictions from the physically based GloFAS model for the two study locations are available from ECMWF (https://www.globalfloods.eu/general-information/data-and-services/). GloFAS forecasts are issued on the first day of every month and consist of 25 ensemble members predicting mean weekly streamflow 17 weeks out from the issue date; only predictions for weeks 1-13 (approximately three months) are retained. A mean bias correction is applied to the GloFAS ensemble mean according to the difference between mean observed and predicted seasonal streamflow across all years. A quantile mapping approach, relating the cumulative distributions functions of observed and predicted streamflow, was also tested (Hashino et al., 2006); however, forecast skill did not substantially differ from the mean bias correction approach. In addition to evaluating the statistical model and GloFAS independently, a multi-model forecast is also constructed utilizing a least squares linear regression to assign weights according to the relative Pearson correlation strength between observed streamflow and each model's predictions (P. J. Block et al., 2009).

3.5 Forecast verification and performance measures

Forecast performance for the three models (statistical, GloFAS, and multi-model) is evaluated at both locations by Pearson
correlation coefficient, Rank Probability Skill Score (RPSS), Probability of Detection (POD), False Alarm Ratio (FAR) and
Threat Score (TS).

RPSS is an extension of the rank probability score (RPS), which measures the categorical accuracy of a forecast (Wilks,
2011). Here, two categories are selected to represent high flow and non-high flow conditions, with the 80th percentile of
observed seasonal streamflow representing the threshold. The RPS is the sum of the squared differences between the forecast
and observed categorical probabilities, and is given as:

$$\text{RPS} = \frac{1}{J-1}\sum_{m=1}^{J} \left[\left(\sum_{j=1}^{m} p_j\right) - \left(\sum_{j=1}^{m} o_j\right)\right]^2, \tag{3}$$

where J is the number of categories, y_j is the forecast probability in the jth category, and o_j is 1 if the event is observed in that
category, otherwise 0. RPS scores range from 0 to 1. RPSS indicates the relative skill of the forecast compared to a
reference forecast and takes the form:

$$\text{RPSS} = 1 - \frac{\text{RPS}}{\text{RPS}_{reference}}. \tag{4}$$

RPSS can vary from -∞ to 1; values above 0 are considered skillful compared to the reference forecast, and a value equal to
1 indicates a perfect categorical forecast. Mean RPSS values across all hindcast years are presented; the reference forecast is
based on historical averages (i.e. climatology).

POD, or "hit rate," describes the fraction of observed extreme (e.g. high flow) events that are correctly predicted and is
calculated as:

$$\text{POD} = \frac{hits}{hits+misses}, \tag{5}$$

where a perfect score is 1 (Wilks, 2011). Because POD can be artificially improved by issuing more extreme predictions, it
must be evaluated in combination with FAR. FAR describes the fraction of predicted extreme events that did not occur, or
"false alarms", calculated as:

$$\text{FAR} = \frac{false\ alarms}{hits\ +false\ alarms}, \tag{6}$$

where a perfect score is 0 (Wilks, 2011).

TS, also called the "critical success index," is the number of predicted extreme events divided by the total number of times
that an extreme event is either predicted or observed, calculated as:

$$\text{TS} = \frac{hits}{hits + misses + false\ alarms}, \tag{7}$$

where a perfect score is 1 (Wilks, 2011). TS is preferred over accuracy (the sum of true positives and true negatives divided by the total number of events) for situations where the extreme category is rarely observed. As previously stated, the extreme

315   category is classified as seasonal streamflow values in the top 20% (80th percentile) of observations.

4 Results

4.1 Large-scale predictor regions

The locations of SST regions that correlate significantly with streamflow vary according to the phase of ENSO (Figure 3). Piura streamflow in El Niño years is positively associated with equatorial Pacific SSTs, encompassing the Niño 1+2 and

320   Niño 3 regions (Figure 3a). This finding aligns with previous work demonstrating that above-average precipitation in northwest Peru is driven primarily by ENSO (e.g., Lagos et al., 2008). Strong El Niño years (e.g. 1983, 1998) have a tendency to lead to extreme flooding in northwest Peru, though floods have also affected the region in other ENSO phases, for example, in 2008, a moderate La Niña ("Emergency Events Database (EM-DAT)," 1988). Piura streamflow variability in neutral and La Niña years is associated with SSTs in the northwest Pacific, north Atlantic, and tropical Indian Oceans

325   (Figure 3a). This is similar to the findings of Bazo et al. (2013) who show an influence of SST anomalies in the tropical Indian and Atlantic Oceans (in addition to the tropical Pacific) on precipitation in northwest Peru.

Marañón streamflow during El Niño years is positively (negatively) associated with northeast Pacific (northwest Atlantic) SSTs (Figure 3b). In La Niña years, when average Marañón streamflow is greater and hydrologic disasters are more common

330   in Amazonian Peru (Rodríguez-Morata et al., 2018), streamflow is associated with SST regions in the tropical Atlantic and Indian Oceans. While El Niño episodes have been linked to below-average precipitation in the Amazon basin (Garreaud et al., 2009; Marengo, 2004), significant teleconnections between equatorial Pacific SSTs and Marañón streamflow are not identified here (Figure 3b).

4.2 Final predictor selection

335   Of the potential predictors listed in Table 2, a subset is selected for each statistical forecast submodel based on correlation significance and model parsimony as described in Section 3 (Table 3). This results in the first PC of statistically significant pre-season SST regions being included in all submodels for both locations. Pre-season streamflow is included in both submodels for Marañón, in line with its greater temporal autocorrelation, while it is included in only the positive phase submodel for Piura. No pre-season precipitation observations are included for Marañón; for Piura the GCM precipitation

340   forecast is included in the negative phase submodel and pre-season observed precipitation is included in the positive and neutral phase submodels.

Natural Hazards
and Earth System
Sciences
Discussions

Table 3: Final predictors included in each submodel. SST PC1 is the first PC of SST regions; F (J) SF is average observed F (J) streamflow (m³/s); Obs Precip is the mean observed JF (J only for Piura) basin-averaged observed precipitation (mm/month); GCM Precip is the FMA precipitation prediction from two NMME members.

Site	Negative Phase Model			Positive Phase Model			Neutral Phase Model		
	Predictors	PCs retained	PC1 % variance explained	Predictors	PCs retained	PC1 % variance explained	Predictors	PCs retained	PC1 % variance explained
Marañón	SST PC1, F SF	1	61	SST PC1, F SF	1	86	-	-	-
Piura	SST PC1, GCM Precip	1	74	SST PC1, J SF, Obs Precip	2	92	SST PC1, Obs Precip	1	88

345

4.3 Statistical model forecasts

The primary focus of this study is to predict occurrence of high flow conditions to initiate flood preparedness actions. The probabilistic statistical forecast model at each location effectively captures interannual variability and extremes (Figs. 4
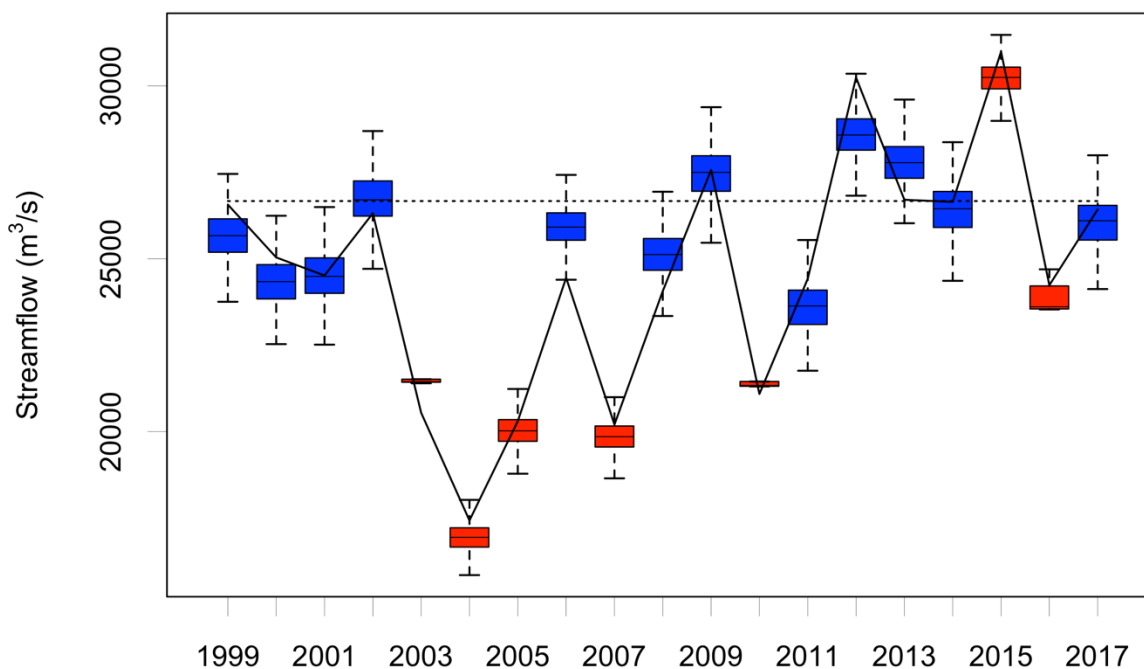
350 **Figure 4:** Marañón River at San Regis MAM streamflow hindcast using the statistical prediction model. The black solid line illustrates observed MAM streamflow; the black dotted line indicates the 80th percentile of MAM observed streamflow. Red (blue) boxes represent years with pre-season El Niño (La Niña) conditions.

and 5). When evaluated categorically, the Marañón forecast model identifies all four high flow years while the forecast for Piura identifies six out of eight (Table 4). El Niño years are associated with lower forecast uncertainty for Marañón; the
355 average standard deviation of error distributions is 42% smaller than in La Niña years. For Piura, La Niña conditions result in lower forecast uncertainty; the average standard deviation of error distributions is 73% larger for years in the neutral phase
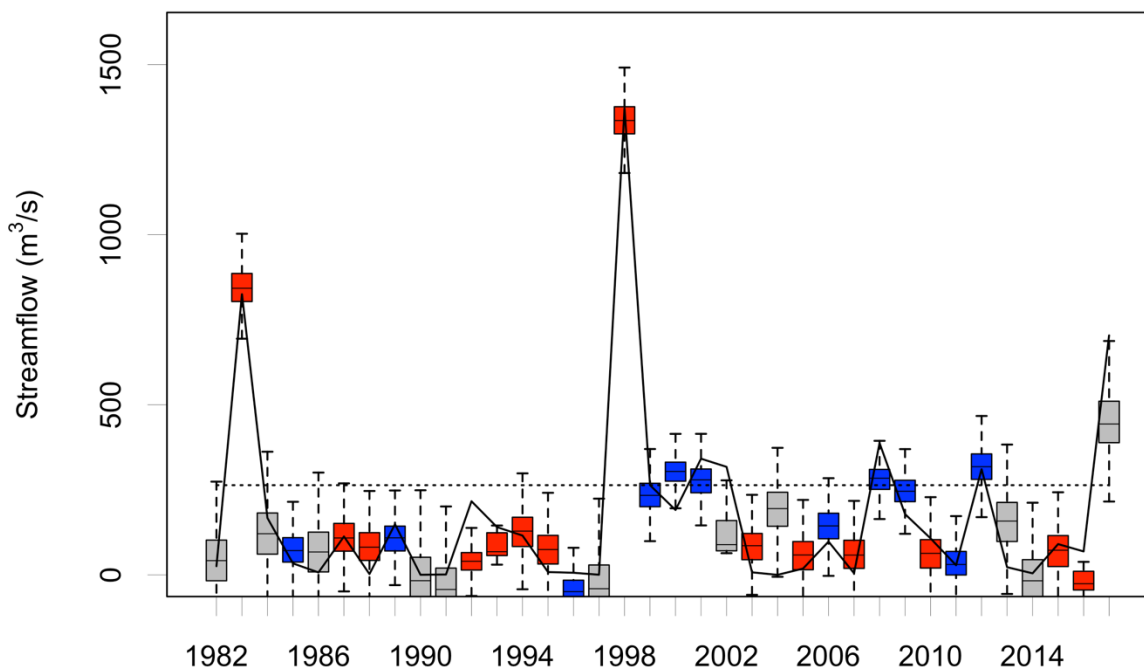
Figure 5: Piura River at Puente Sánchez Cerro FMA streamflow hindcast using the statistical prediction model. The black solid line illustrates observed FMA streamflow; the black dotted line indicates the 80th percentile of FMA observed streamflow. Red (blue) boxes
360 represent years with pre-season El Niño (La Niña) conditions.

Table 4: Contingency table for statistical, GloFAS, and multi-model predictions of high flow (top 20%) and low flow (bottom 80%) MAM (FMA) streamflow for the Marañón (Piura) River.

			Observed Conditions					
			Statistical		GloFAS		Multi-model	
			Low	High	Low	High	Low	High
Predicted Conditions	**Marañón**	Low	14	0	13	2	15	0
		High	1	4	2	2	0	4
	Piura	Low	27	2	27	5	28	4
		High	1	6	1	3	0	4

365 and 17% larger in El Niño years. Despite low streamflow in many years, the forecast model for Piura captured the approximate magnitude of the top three extremes in 1983, 1998 and 2017 (Figure 5). An analysis of flood reports from news media and global disaster databases including EM-DAT and the Dartmouth Flood Observatory indicate that flooding along the Piura River occurred in each of these years, though not necessarily at the station itself.

4.4 Multi-model forecasts

370 For the multi-model forecast, least squares weighting results in a significantly higher weight (83% and 72% for the Marañón and Piura, respectively) assigned to the statistical model and therefore multi-model Pearson correlation and RPSS values are similar to the independent statistical forecast model (Table 5). The Marañón multi-model detects all four true positives in the upper category – two more than GloFAS and the same as the statistical model. The Piura multi-model detects four true positives, two fewer than the statistical model and one more than GloFAS. For both Piura and Marañón, the multi-model
375 forecast improves POD, FAR and TS compared to GloFAS (Table 6).

Table 5: Mean RPSS and Pearson correlation coefficients for each location and forecast approach.

Site	Predictand	Statistical		GloFAS		Multi-model	
		RPSS	Pearson Correlation	RPSS	Pearson Correlation	RPSS	Pearson Correlation
Marañón	**MAM streamflow**	0.84	0.97	0.25	0.84	0.83	0.98
Piura	**FMA streamflow**	0.61	0.95	0.18	0.91	0.57	0.95

Table 6: Same as Table 5, but for POD, FAR and TS.

Site	Predictand	Statistical			GloFAS			Multi-model		
		POD	FAR	TS	POD	FAR	TS	POD	FAR	TS
Marañón	**MAM streamflow**	1	0.2	0.8	0.5	0.5	0.33	1	0	1
Piura	**FMA streamflow**	0.75	0.14	0.67	0.38	0.25	0.33	0.5	0	0.5

380

5 Discussion

5.1 Triggering early action

While verification metrics offer useful ways to evaluate forecast performance, a forecast's true value is determined by the end user (Hartmann et al., 2002). Because floods are the main hydro-meteorological threat in the Peruvian Amazon (IFRC,

385   2019) and Piura basins, correctly predicting the years with high seasonal streamflow are of outsized importance compared to predicting low-flow years. The Peruvian Red Cross early action protocol steps for flooding are triggered when a forecast predicts a 75% chance (probability) of streamflow above the 80th percentile (threshold). This criterion is applied to the three forecasts (statistical model, GloFAS, and multi-model) to understand when actions would be triggered based on each forecast at San Regis on the Marañón River and at Puente Sánchez Cerro on the Piura River.

390

Based on this criteria, four years in the historical record qualify for early action at San Regis (2009, 2012, 2013, 2015). Out of these four, the statistical model predicts action in all four years and GloFAS in two (2009 and 2012) (Figure 6). While an
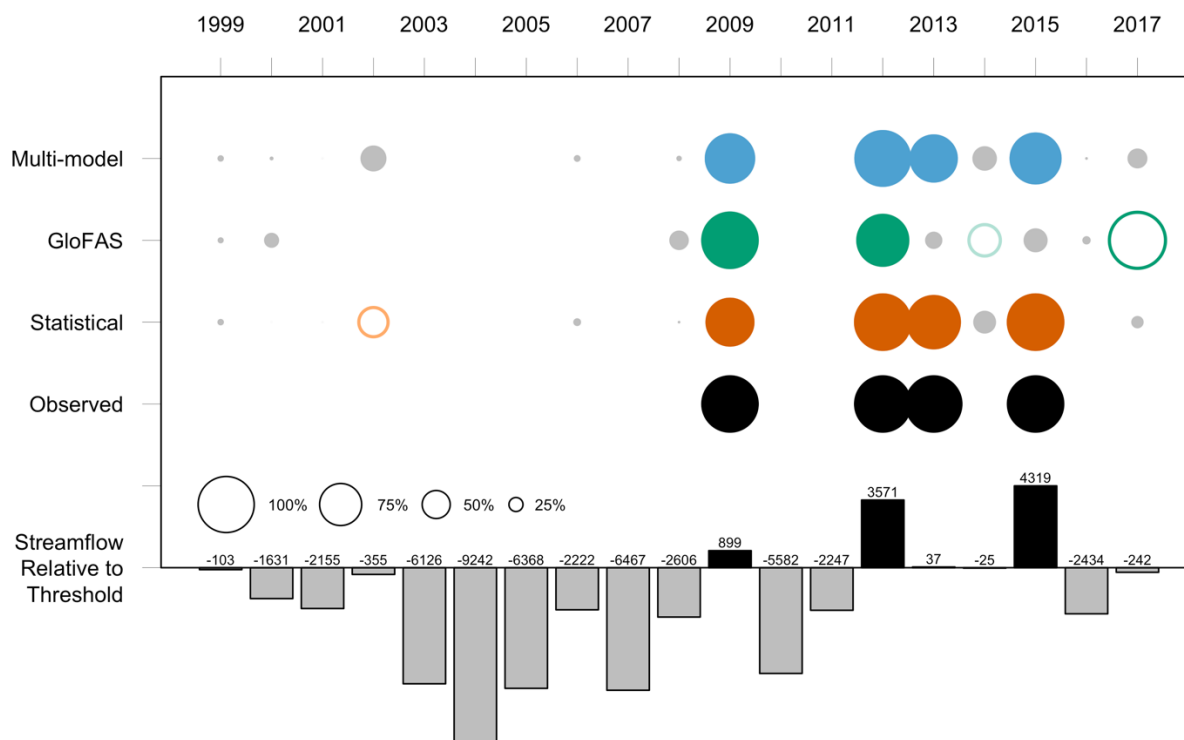
Figure 6: Marañón River at San Regis early actions triggered (≥75% probability of exceeding threshold) based on observed data (black)

395   and season-ahead predictions from: statistical model (orange), GloFAS (green), and multi-model (blue). Dark colors represent a ≥75% probability of threshold exceedance; light colors represent a 50-75% probability of threshold exceedance; grey represents a <50% probability of threshold exceedance. Open circles represent false positives. Circle sizes are scaled to probability of threshold exceedance. Black (grey) bars indicate relative magnitude of streamflow compared to 80th percentile in m³/s.

17

observed trigger does not necessitate observed flooding or flood impacts, the Centre for Research on the Epidemiology of
400   Disasters (CRED) Emergency Events Database (EM-DAT) provides evidence of flooding in the western Amazon (Loreto
region), though not necessarily on the Marañón, in 2012, 2013 and 2015 (the three highest seasonal averages on record)
suggesting that early actions in these years could be warranted. In 2012 and 2015, when Marañón observed streamflow
exceeds the threshold required for early action (26,671 m³/s) by over 3500 m³/s, the statistical model triggers with a 100%
probability of threshold exceedance in both cases. In 2013, when observed streamflow is just 37 m³/s above the threshold,
405   the statistical model predicts a 94.3% probability of threshold exceedance while the following year, when streamflow is 25
m³/s below the threshold, the statistical model predicts a 37.9% probability. GloFAS correctly triggers early action in 2009
and 2012 with 100% and 92% probabilities of threshold exceedance respectively while missing in 2013 and 2015 with
predictions of 28% and 40% exceedance. In two out of the four years with observed triggers, the statistical model and
GloFAS threshold exceedance probabilities differ by at least 60 percentage points (Figure 6). Additionally, in 2017, when
410   streamflow misses the threshold for early action by only 242 m³/s, the two models differ in their predicted probability of
threshold exceedance by 81 points. Collectively, these differences suggest that the two models capture distinct signals in
years critical for disaster preparedness. However, the multi-model least-squares ensemble forecast, weighted heavily toward
the statistical model, mirrors the latter's predictions (Figure 6).

415   At Puente Sánchez Cerro, all models trigger early actions during the three largest events in 1983, 1998 and 2017 – each of
which resulted in significant impacts in the Piura River basin, collectively killing over 1000 people and affecting another 3.6
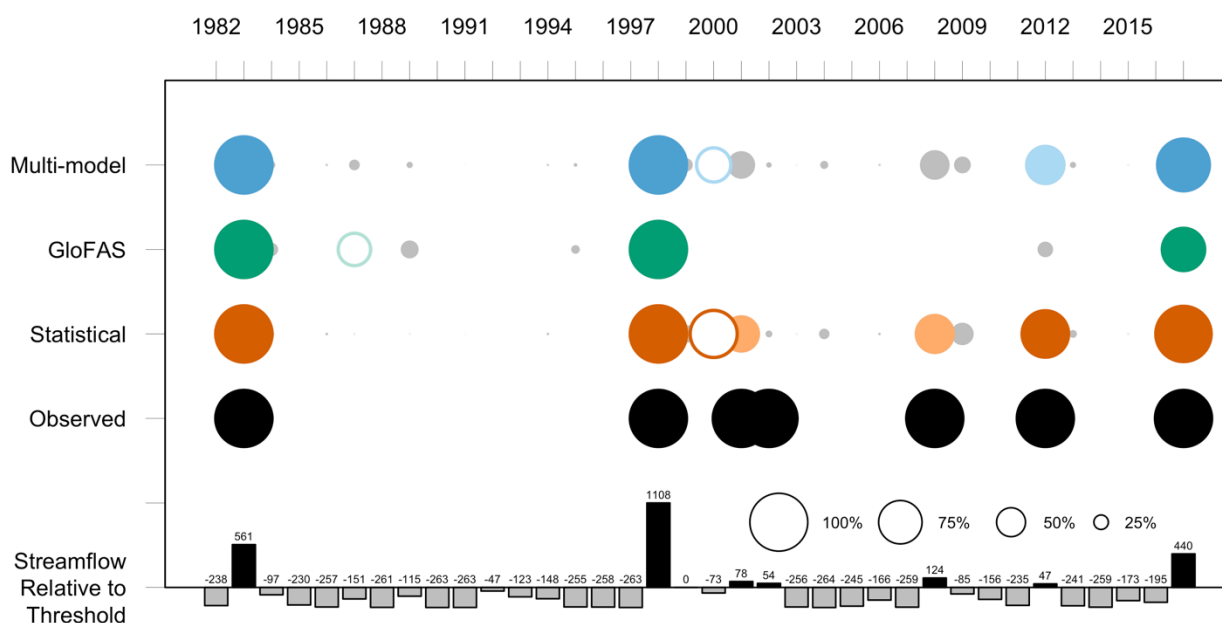
Figure 7: Same as Figure 6 for Piura River at Puente Sánchez Cerro.

420   million (Caviedes, 1984; "Emergency Events Database (EM-DAT)," 1988; *Peru - Floods Fact Sheet #1, Fiscal Year (FY) 1998*, 1998; "Peru floods: Four killed as Piura bursts its banks," 2017; French & Mechler, 2017) (Figure 7). The statistical model included one false positive in 2000 with an 81.3% predicted probability of exceedance (observed streamflow was at the 74th percentile). Additional historical years (2001, 2002, 2008 and 2012) also meet the criteria for early action with evidence of flooding in the Piura province, collectively resulting in 60 deaths and affecting 508,000 people ("Emergency

425   Events Database (EM-DAT)," 1988), although streamflow magnitudes were substantially lower. Of these the statistical model captured one (2012) while GloFAS failed to capture any. A modified trigger mechanism enables capturing some of these lower-magnitude events without additional false positives; if early action is triggered based on just a 50% probability of exceeding the 80th percentile, the statistical model also triggers in 2001 and 2008 (thus capturing 6 of the 7 observed events). However, this study forgoes any systematic attempt to assess when early actions may or may not be warranted (e.g.

430   determining an optimal threshold) in favor of illustrating that additional skill in detecting observed early action triggers is possible with the use of tailored statistical and multi-model forecasts. Further refinement of effective trigger levels also requires understanding regionally specific flood impacts and expected benefits of early action.

5.2 Varying the probability required to trigger action

The trigger mechanism for early action, which requires a 75% probability of streamflow above the 80th percentile, suggests a

435   tolerance for a FAR of 0.25 for an unbiased forecast. Indeed, the tolerance for false positives when implementing early action is an open question for decision makers and may depend on numerous technical, institutional and political factors. In both locations, the probability of exceeding this threshold can be reduced significantly below 75% while remaining at or below an acceptable FAR, thereby enabling the forecasts to capture additional high-flow events. At Puente Sánchez Cerro, lowering the probability can lead to the capture of six out of seven events by the statistical and multi-model forecasts

440   (improving from 4 and 3 events at the 75% probability, respectively) while still maintaining a low FAR (Figure 8b and 8d). At San Regis the statistical and multi-model approaches both detect all four triggers at 75% probability, but no additional false positives are introduced by either forecast until the required trigger probability is reduced to approximately 50% (Figure 8c). For GloFAS, the benefit of additional events captured is not realized until the required trigger probability is well below 50% (Figure 8a and 8b), at which point the FAR is above 0.25 (Figure 8c and 8d). False positives incurred by

445   reducing the trigger probability may also be offset by a stopping mechanism in which action is halted if the forecast is not confirmed 30 days later (IFRC, 2019).

Threat Score (TS), a validation metric that describes the degree to which triggering of observed events corresponds to triggering of events based on forecasts, is one method to evaluate the benefits of additional true positives against the costs of

450   additional false positives when true positives are relatively rare. TS is maximized from 53% to 84% (36% to 61%) and 44% to 83% (27% to 44%) respectively for the statistical and multi-model approaches for Marañón (Piura) (Figure 8e and 8f). By comparison, TS for GloFAS is nearly always lower and generally less variable, reaching its maximum of 0.57 (0.44) from
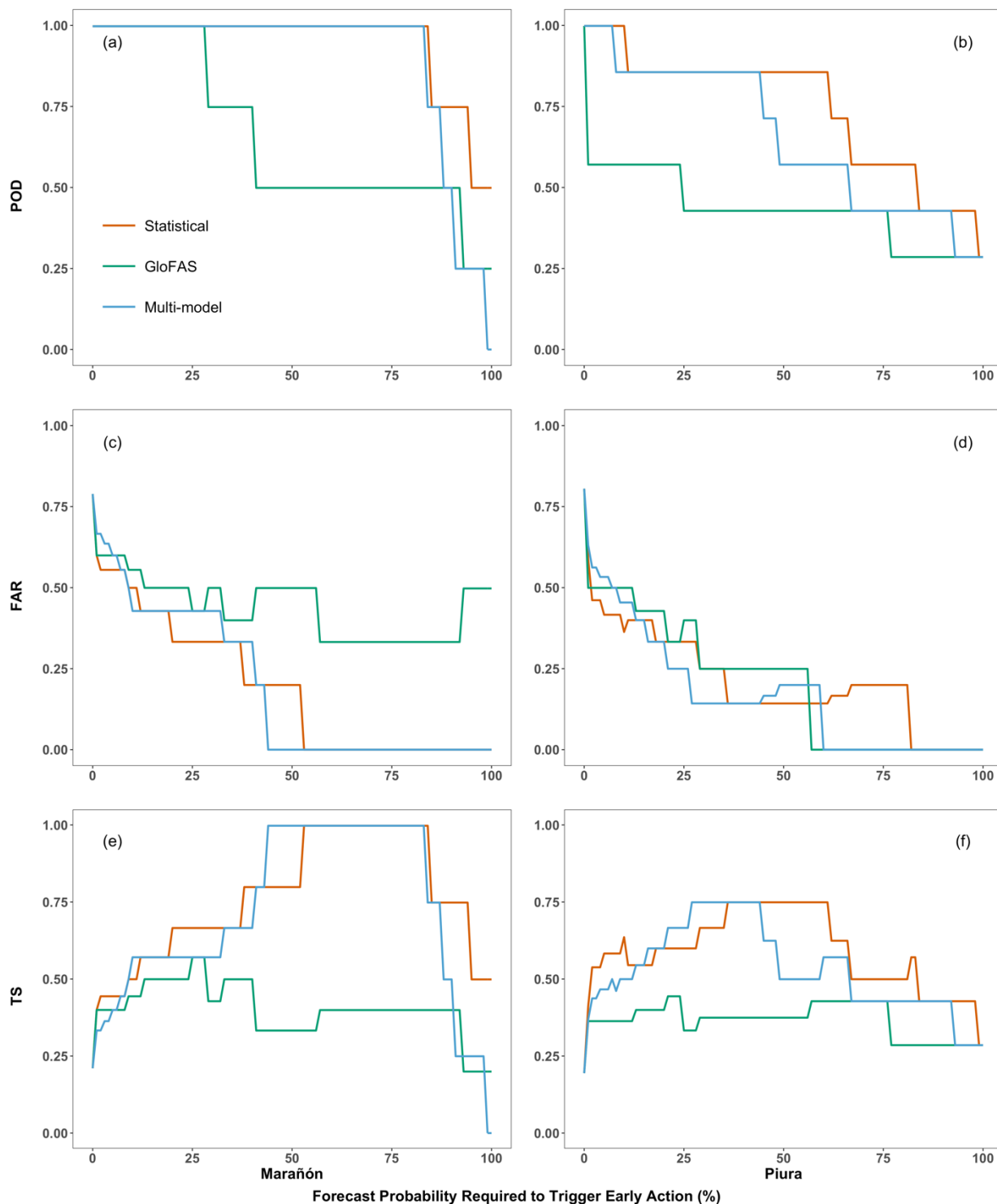
Figure 8: Probability of detection (POD), false alarm ratio (FAR) and threat score (TS) as a function of the threshold probability required
455   to trigger early action for each location and forecast approach.

Natural Hazards
and Earth System
Sciences
Discussions
EGU
Open Access

25% to 28% (21% to 24%) for Marañón (Piura). Thus, a 75% required trigger probability tends to be a relatively strict level, as it often significantly surpasses the required trigger probability yielding the highest TS.

5.3 Implications of binary trigger mechanism

The binary nature of the trigger mechanism is vulnerable to situations where similar observed conditions result in early
460 action in one instance but not in another. Marañón River streamflow, which averages 24,600 m³/s during the MAM season, exceeded the 80th percentile by substantial margins in 2012 and 2015 (3,571 m³/s and 4,319 m³/s respectively), while in 2009 and 2013 it exceeded the 80th percentile by just 899 m³/s and 37 m³/s, respectively (Figs. 4 and 6). On the other hand, in 2014, streamflow averaged just 25 m³/s (0.09%) below the 80th percentile – warranting no early action based on the trigger criteria. Similar effects are visible in Figs. 5 and 7 for the Piura River: in 1999, streamflow was exactly equal to the 80th
465 percentile and so did not count as an observed trigger (the stated mechanism requires that streamflow *exceed* the 80th percentile). From an operational standpoint, such edge cases beg the question: should some amount of early action still occur? Absent a direct physical basis underpinning the streamflow magnitude required to trigger early action (e.g. setting a threshold based on when a levee begins to overtop), two events of similar magnitude – one slightly above and one below the threshold – are likely to produce similar impacts with early actions likely to yield similar benefits. Moreover, early action in
470 response to two such events may suggest that the action taken "in vain" yields fewer or no benefits compared to actions initiated in response to a true positive. For example, when GloFAS triggers early action for the Marañón River in 2017 (Figure 6), this is considered a false positive despite observed conditions falling less than 1% below the threshold, illustrating a potential weakness of both the trigger mechanism and categorical evaluation of forecasts in general. This reinforces the need to also evaluate forecasts with complementary performance measures paired with local contextual
475 knowledge. A modified trigger approach could incorporate multiple tiers of early actions triggered by increasing levels of forecast confidence. Likewise, if forecast confidence later decreases, a tiered stopping mechanism could halt actions in reverse order.

6 Conclusion

This paper describes a method by which locally-tailored season-ahead statistical forecasts can improve the detection of
480 trigger-based early actions and is illustrated with a case study for two sites in Peru. The statistical forecast developed in this study – as well as a multi-model ensemble forecast composed of the statistical and an operational physically-based model – consistently outperform the aforementioned physically-based model for both study locations. Detection of additional high-flow events is possible by lowering the forecast probability required to trigger actions while maintaining a low false alarm ratio.

485

While higher seasonal average streamflow values typically imply a greater probability of both flooding and the need for early action, lower seasonal average streamflow values may obscure high daily peaks that nonetheless result in flood impacts. Thus, even a perfect seasonal forecast may not reflect all instances where early action is justified. Additionally, because the statistical model developed here is optimized for performance across all years, further refinement prioritizing the

490   detection of appropriate trigger levels for early action in high flow years may be warranted. Such efforts could involve alternative modeling frameworks (e.g. logistic regression), additional predictors, and evaluation of category selection applied in the prediction process.

Code availability. Code used in this study is available upon request.

495

Data availability. Streamflow data used in this study are from SENAMHI. While the dataset is not public, it may be made available upon request. PISCO precipitation data are available at piscoprec.github.io. Climate data obtained from NOAA are available at noaa.gov.

500   *Author contributions*. PB was responsible for conceptualization. CK developed and evaluated the prediction model with input from PB and DL. JB facilitated access to project resources (including datasets and documents) and provided contextual information. CK prepared the manuscript with editing contributions from all authors. PB and DL were responsible for project administration and PB was responsible for funding acquisition.

505   *Competing interests*. The authors declare that they have no conflict of interest.

515

Natural Hazards
and Earth System
Sciences
Discussions

Open Access

References

Aguirre, J., De La Torre Ugarte, D., Bazo, J., Quequezana, P. and Collado, M.: Evaluation of early action mechanisms in Peru regarding preparedness for El Niño, Int. J. Disaster Risk Sci., 10(4), 493–510, doi:10.1007/s13753-019-00245-x, 2019.

520 Aybar, C., Fernández, C., Huerta, A., Lavado, W., Vega, F. and Felipe-Obando, O.: Construction of a high-resolution gridded rainfall dataset for Peru from 1981 to the present day, Hydrol. Sci. J., 65(5), 770–785, doi:10.1080/02626667.2019.1649411, 2020.

Badr, H. S., Zaitchik, B. F. and Guikema, S. D.: Application of statistical models to the prediction of seasonal rainfall anomalies over the Sahel, J. Appl. Meteorol. Climatol., 614–636, doi:10.1175/JAMC-D-13-0181.1, 2013.

525 Bayer, A. M., Danysh, H. E., Garvich, M., Gonzálvez, G., Checkley, W., Álvarez, M. and Gilman, R. H.: An unforgettable event: a qualitative study of the 1997 – 98 El Niño in northern Peru, Disasters, 38(2), 351–375, doi:10.1111/disa.12046, 2014.

Bazo, J., de las Nieves Lorenzo, M. and Porfirio da Rocha, R.: Relationship between monthly rainfall in NW Peru and tropical sea surface temperature, Adv. Meteorol., 1–9, doi:10.1155/2013/152875, 2013.

530 Bazo, J., Singh, R., Destrooper, M. and Coughlan de Perez, E.: Pilot experiences in using seamless forecasts for early action: The "ready-set-go!" approach in the Red Cross, in Sub-seasonal to Seasonal Prediction, pp. 387–398, Elsevier., 2019.

Bischiniotis, K., van den Hurk, B., Zsoter, E., Coughlan De Perez, E., Grillakis, M. and Aerts, J. C. J. H.: Evaluation of a global ensemble flood prediction system in Peru, Hydrol. Sci. J., 64(10), 1171–1189, doi:10.1080/02626667.2019.1617868, 2019.

535 Block, P. and Rajagopalan, B.: Interannual variability and ensemble forecast of upper Blue Nile basin Kiremt, J. Hydrometeorol., 8, 327–343, doi:10.1175/JHM580.1, 2007.

Block, P. and Rajagopalan, B.: Statistical – dynamical approach for streamflow modeling at Malakal, Sudan, on the White Nile River, J. Hydrol. Eng., 185–196, doi:10.1061/(ASCE)1084-0699(2009)14:2(185), 2009.

Block, P. J., Assis, F., Filho, S., Sun, L. and Kwon, H.: A streamflow forecasting framework using multiple climate and 540 hydrological models, J. Am. Water Resour. Assoc., 45(4), 828–843, doi:10.1111/j.1752-1688.2009.00327.x, 2009.

Braman, L. M., Aalst, M. K. Van, Mason, S. J., Suarez, P., Ait-Chellouche, Y. and Tall, A.: Climate forecasts in disaster management: Red Cross flood operations in West Africa, 2008, Disasters, 37(1), 144–164, doi:10.1111/j.1467-7717.2012.01297.x, 2013.

Cabot Venton, C., Fitzgibbon, C., Shitarek, T., Coulter, L. and Dooley, O.: The Economics of Early Response and Disaster 545 Resilience: Lessons from Kenya and Ethiopia, London., 2012.

Caviedes, C. N.: El Niño 1982-83, Geogr. Rev., 74(3), 267–290, 1984.

Doocy, S., Daniels, A., Murray, S. and Kirsch, T. D.: The human impact of floods: a historical review of events 1980-2009 and systematic literature review, PLOS Curr. Disasters, doi:10.1371/currents.dis.f4deb457904936b07c09daa98ee8171a, 2013.

550 Emergency Events Database (EM-DAT), [online] Available from: https://www.emdat.be/ (Accessed 3 March 2020a), 1988.

Emerton, R., Zsoter, E., Arnal, L., Cloke, H. L., Muraro, D., Prudhomme, C., Stephens, E. M., Salamon, P. and Pappenberger, F.: Developing a global operational seasonal hydro-meteorological forecasting system: GloFAS-Seasonal v1.0, Geosci. Model Dev., 11, 3327–3346, doi:10.5194/gmd-11-3327-2018, 2018.

Equatorial Pacific Sea Surface Temperatures, NOAA Natl. Centers Environ. Inf. [online] Available from: 555 https://www.ncdc.noaa.gov/teleconnections/enso/indicators/sst/ (Accessed 10 May 2020b), n.d.

Espinoza Villar, J. C., Guyot, J. L., Ronchail, J., Cochonneau, G., Filizola, N., Fraizy, P., Labat, D., de Oliveira, E., Ordoñez, J. J. and Vauchel, P.: Contrasting regional discharge evolutions in the Amazon basin (1974–2004), J. Hydrol., doi:10.1016/j.jhydrol.2009.03.004, 2009.

Fan, Y. and van den Dool, H.: Climate Prediction Center global monthly soil moisture data set at 0.5° resolution for 1948 to 560 present, J. Geophys. Res., 109, 1–8, doi:10.1029/2003JD004345, 2004.

French, A. and Mechler, R.: Managing El Niño Risks Under Uncertainty in Peru: Learning from the past for a more disaster-resilient future, Laxenburg, Austria., 2017.

Funk, C., Peterson, P., Landsfeld, M., Pedreros, D., Verdin, J., Shukla, S., Husak, G., Rowland, J., Harrison, L., Hoell, A. and Michaelsen, J.: The climate hazards infrared precipitation with stations — a new environmental record for monitoring extremes, Sci. Data, 1–21, doi:10.1038/sdata.2015.66, 2015.

Gámiz-Fortis, S. R., Esteban-Parra, M. J., Trigo, R. M. and Castro-Díez, Y.: Potential predictability of an Iberian river flow based on its relationship with previous winter global SST, J. Hydrol., 385, 143–149, doi:10.1016/j.jhydrol.2010.02.010, 2010.

Garreaud, R. D., Vuille, M., Compagnucci, R. and Marengo, J.: Present-day South American climate, Palaeogeogr. Palaeoclimatol. Palaeoecol., 281, 180–195, doi:10.1016/j.palaeo.2007.10.032, 2009.

Giuliani, M., Zaniolo, M., Castelletti, A., Davoli, G. and Block, P.: Detecting the state of the climate system via artificial intelligence to improve seasonal forecasts and inform reservoir operations, Water Resour. Res., 9133–9147, doi:10.1029/2019WR025035, 2019.

Golnaraghi, M.: Institutional Partnerships in Multi-Hazard Early Warning Systems: A Compilation of Seven National Good Practices and Guiding Principles, Springer, New York., 2012.

Gros, C., Bailey, M., Schwager, S., Hassan, A., Zingg, R., M, U. M., Shahjahan, M., Islam, H., Lux, S., Jaime, C. and Coughlan de Perez, E.: Household-level effects of providing forecast-based cash in anticipation of extreme weather events: Quasi-experimental evidence from humanitarian interventions in the 2017 floods in Bangladesh, Int. J. Disaster Risk Reduct., 41, 1–11, doi:10.1016/j.ijdrr.2019.101275, 2019.

Harriman, L.: Cyclone Phailin in India: Early warning and timely actions saved lives, Environ. Dev., 9, 93–100, doi:10.1016/j.envdev.2013.12.001, 2014.

Hartmann, H., Pagano, T., Sorooshian, S. and Bales, R.: Confidence builders: evaluating seasonal climate forecasts from user perspectives, Bull. Am. Meteorol. Soc., (May), 683–698, doi:10.1175/1520-0477(2002)083<0683:CBESCF>2.3.CO;2, 2002.

Hashino, T., Bradley, A. A. and Schwartz, S. S.: Evaluation of bias-correction methods for ensemble streamflow volume forecasts, Hydrol. Earth Syst. Sci. [online] Available from: www.hydrol-earth-syst-sci.net/11/939/2007/, 2006.

IFRC: DREF operation update Peru: Floods., 2012.

IFRC: Emergency Plan of Action (EPoA) Peru: Flood., 2015.

IFRC: Peru: Floods in the lower Amazon jungle early action protocol summary., 2019.

IFRC: World disasters report 2020, Geneva., 2020.

Infanti, J. and Kirtman, B.: Southeastern U.S. rainfall prediction in the North American Multi-Model Ensemble, J. Hydrometeorol., 15, 529–550, doi:10.1175/JHM-D-13-072.1, 2014.

Ionita, M., Dima, M., Lohmann, G., Scholz, P. and Rimbu, N.: Predicting the June 2013 European flooding based on precipitation, soil moisture, and sea level pressure, J. Hydrometeorol., (April), 598–614, doi:10.1175/JHM-D-14-0156.1, 2015.

Kalnay, E., Kanamitsu, M., Kistler, R., Collins, W., Deaven, D., Gandin, L., Iredell, M., Saha, S., White, G., Woollen, J., Zhu, Y., Chelliah, M., Ebisuzaki, W., Higgins, W., Janowiak, J., Mo, K. C., Ropelewski, C., Wang, J., Leetmaa, A., Reynolds, R., Jenne, R. and Joseph, D.: The NCEP/NCAR 40-Year Reanalysis Project, Bull. Am. Meteorol. Soc., 437–472, 1996.

Kirtman, B., Min, D., Infanti, J., Kinter III, J., Paolino, D., Zhang, Q., Dool, H., Saha, S., Mendez, M. P., Becker, E., Peng, P., Tripp, P., Merryfield, W., Denis, B. and Wood, E.: The North American Multimodel Ensemble, Bull. Am. Meteorol. Soc., (April), 585–602, doi:10.1175/BAMS-D-12-00050.1, 2014.

Kvist, L. P. and Nebel, G.: A review of Peruvian flood plain forests: ecosystems, inhabitants and resource use, For. Ecol. Manage., 3–26, doi:10.1016/S0378-1127(00)00679-4, 2001.

Lagos, P., Silva, Y., Nickl, E. and Mosquera, K.: El Niño? related precipitation variability in Perú, Adv. Geosci., 231–237 [online] Available from: https://hal.archives-ouvertes.fr/hal-00297103, 2008.

Lee, D., Ward, P. and Block, P.: Defining high-flow seasons using temporal streamflow patterns from a global model, Hydrol. Earth Syst. Sci., 19(11), 4689–4705, doi:10.5194/hess-19-4689-2015, 2015.

Lee, D., Ward, P. J. and Block, P. J.: Attribution of large-scale climate patterns to seasonal peak-flow and prospects for prediction globally, Water Resour. Res., 1–23, doi:10.1002/2017WR021205, 2018.

Lopez, A., Coughlan de Perez, E., Bazo, J., Suarez, P., van den Hurk, B. and van Aalst, M.: Bridging forecast verification and humanitarian decisions: A valuation approach for setting up action-oriented early warnings, Weather Clim. Extrem., 27(April 2016), 100167, doi:10.1016/j.wace.2018.03.006, 2019.

Marengo, J. A.: Interdecadal variability and trends of rainfall across the Amazon basin, Theor. Appl. Climatol., 79–96, doi:10.1007/s00704-004-0045-8, 2004.

Munich RE: Natural catastrophes 2011: Analyses, assessments, positions., 2012.

Munich RE: Natural catastrophes 2017: A stormy year., 2018.

Perez, E. C. De, Hurk, B. Van Den, Aalst, M. K. Van, Amuron, I. and Bamanya, D.: Action-based flood forecasting for triggering humanitarian action, Hydrol. Earth Syst. Sci., 20, 3549–3560, doi:10.5194/hess-20-3549-2016, 2016.

Peru - Floods Fact Sheet #1, Fiscal Year (FY) 1998, [online] Available from: https://reliefweb.int/report/peru/peru-floods-fact-sheet-1-fiscal-year-fy-1998 (Accessed 6 May 2020), 1998.

Peru floods: Four killed as Piura bursts its banks, BBC News [online] Available from: https://www.bbc.com/news/world-latin-america-39418314 (Accessed 21 May 2020), 2017.

Public Health London: Heatwave plan for England. [online] Available from: https://assets.publishing.service.gov.uk/government/uploads/system/uploads/attachment_data/file/888668/Heatwave_plan_for_England_2020.pdf, 2018.

Ramirez, I. J. and Briones, F.: Understanding the El Niño Costero of 2017: The definition problem and challenges of climate forecast and disaster responses, Int. J. Disaster Risk Sci., 489–492, doi:10.1007/s13753-017-0151-8, 2017.

Rodríguez-Morata, C., Ballesteros-canovas, J., Rohrer, M., Espinoza, J. C., Beniston, M. and Stoffel, M.: Linking atmospheric circulation patterns with hydro-geomorphic disasters in Peru, Int. J. Climatol., 3388–3404, doi:10.1002/joc.5507, 2018.

Rodriguez, R., Mabres, A., Luckman, B., Evans, M., Masiokas, M. and Ektvedt, T. M.: "El Niño" events recorded in dry-forest species of the lowlands of northwest Peru, Dendrochronologia, 22, 181–186, doi:10.1016/j.dendro.2005.05.002, 2005.

Smith, T. M., Reynolds, R. W., Peterson, T. C. and Lawrimore, J.: Improvements to NOAA's historical merged land – ocean surface temperature analysis (1880 – 2006), J. Clim., 2283–2296, doi:10.1175/2007JCLI2100.1, 2008.

Stephens, E., Day, J. J., Pappenberger, F. and Cloke, H.: Precipitation and floodiness, Geophys. Res. Lett., 316–323, doi:10.1002/2015GL066779.Received, 2015.

Takahashi, K. and Martínez, A. G.: The very strong coastal El Niño in 1925 in the far-eastern Pacific, Clim. Dyn., 52(12), 7389–7415, doi:10.1007/s00382-017-3702-1, 2017.

Tanner, T., Gray, B., Guigma, K., Iqbal, J., Levine, S., Macleod, D., Nahar, K., Rejve, K. and Venton, C. C.: Scaling up early action. Lessons, challenges and future potential in Bangladesh, London., 2019.

Towner, J., Cloke, H. L., Lavado, W., Santini, W., Bazo, J., Coughlan de Perez, E. and Stephens, E. M.: Attribution of Amazon floods to modes of climate variability: A review, Meteorol. Appl., doi:10.1002/met.1949, 2020.

Venkateswaran, K., MacClune, K. and Enriquez, M. .: Learning from El Niño Costero 2017: Opportunities for building resilience in Peru., 2017.

Wang, F. and Vavrus, S.: No Title., 2020.

Wilkinson, E., Weingärtner, L., Choularton, R., Bailey, M., Todd, M., Kniveton, D. and Venton, C. C.: Forecasting hazards, averting disasters. Implementing forecast-based early action at scale, London., 2018.

Wilks, D.: Statistical methods in the atmospheric sciences, Academic Press., 2011.

Wolter, K. and Timlin, M. S.: El Niño/Southern Oscillation behaviour since 1871 as diagnosed in an extended multivariate ENSO index (MEI.ext), Int. J. Climatol., 1074–1087, doi:10.1002/joc.2336, 2011.

World Disasters Report 2009: Focus on early warning, early action., 2009.

Wu, S., Notaro, M., Vavrus, S., Mortensen, E., Montgomery, R., Piérola, J. de and Block, P.: Efficacy of tendency and linear inverse models to predict southern Peru's rainy season precipitation, Int. J. Climatol., 2590–2604, doi:10.1002/joc.5442, 2018.

Zhou, J. and Lau, K.-M.: Does a monsoon climate exist over South America?, J. Clim., 1020–1040, doi:10.1175/1520-0442(1998)011<1020:DAMCEO>2.0.CO;2, 1998.

Zimmerman, B. G., Vimont, D. J. and Block, P. J.: Utilizing the state of ENSO as a means for season-ahead predictor selection, Water Resour. Res., 3761–3774, doi:10.1002/2015WR017644, 2016.